applied optics

Derivation of the correlation diffusion equation with static background and analytical solutions

Tiziano Binzoni,[1,2,*] André Liemert,[3] Alwin Kienle,[3] and Fabrizio Martelli[4]

[1]Département de Neurosciences Fondamentales, University of Geneva, 1205 Geneva, Switzerland
[2]Département de l'Imagerie et des Sciences de l'Information Médicale, University Hospital, 1211 Geneva 4, Switzerland
[3]Institut für Lasertechnologien in der Medizin und Meßtechnik, Helmholtzstraße 12, D-89081 Ulm, Germany
[4]Dipartimento di Fisica e Astronomia dell'Università degli Studi di Firenze, 50019 Sesto Fiorentino, Firenze, Italy
*Corresponding author: tiziano.binzoni@unige.ch

Received 26 October 2016; revised 16 December 2016; accepted 18 December 2016; posted 19 December 2016 (Doc. ID 279576); published 24 January 2017

A new correlation diffusion equation has been derived from a correlation transport equation allowing one to take into account the presence of moving scatterers and static background. Solutions for the reflectance from a semi-infinite medium have been obtained (point-like and ring detectors). The solutions have been tested by comparisons with "gold standard" Monte Carlo (MC) simulations. These formulas suitably describe the electric field autocorrelation function, for Brownian or random movement of the scatterers, even in the case where the probability for a photon to interact with a moving scatterer is very low. The proposed analytical models and the MC simulations show that the "classical" model, often used in diffuse correlation spectroscopy, underestimates the normalized field autocorrelation function for increasing correlation times.

OCIS codes: (170.0170) Medical optics and biotechnology; (170.3660) Light propagation in tissues; (170.3340) Laser Doppler velocimetry; (290.5825) Scattering theory.

https://doi.org/10.1364/AO.56.000795

1. INTRODUCTION

The knowledge of the electric field autocorrelation function of a laser light that has traveled into a biological tissue allows one to estimate tissue blood flow [1–5]. For this reason, if one wants to extract reliable blood-flow information from the experimental data, it is essential to define precise mathematical models for the autocorrelation function. Today, from a strictly practical point of view, a unique "classical" model for the field autocorrelation function, $G_{1\text{class}}(\rho,\tau)$ (Wmm^{-2}), is used (see, e.g., [3,6])

$$G_{1\text{class}}(\rho,\tau)=S_0\frac{3\mu_s'}{4\pi}\left(\frac{e^{-Kr_1}}{r_1}-\frac{e^{-Kr_2}}{r_2}\right), \tag{1}$$

which holds for a unitary isotropic-emitting point light source of 1 Wmm^{-3} sr^{-1}, where $S_0=1$ W. Equation (1) is considered to hold for a semi-infinite medium, containing moving scatterers (mainly red blood cells) in a static background, and in reflectance geometry. The variable ρ (mm) represents the source/detector spacing and τ (s) the correlation time. The constant K is expressed as

$$K^2=3\mu_a\mu_s'+P_m\mu_s'^2a, \tag{2}$$

where

$$a=\frac{1}{3}\left(\frac{2\pi n}{\lambda}\right)^2\langle\Delta r^2(\tau)\rangle; \tag{3}$$

μ_s' (mm^{-1}) is the reduced scattering coefficient, μ_a (mm^{-1}) the absorption coefficient, $P_m\in[0,1]$ the probability that a scatterer is moving, λ (mm) the laser wavelength (continuous wave), and n the refractive index of the medium. The refractive index of the external medium (air) is always set to 1. The constant r_1 and r_2 are expressed as

$$r_1=(\rho^2+z_{0t}^2)^{1/2}, \tag{4}$$

$$r_2=[\rho^2+(z_{0t}+2z_{et})^2]^{1/2}, \tag{5}$$

and

$$z_{et}=2AD, \tag{6}$$

$$z_{0t}=\frac{1}{\mu_s'}, \tag{7}$$

$$D=\frac{1}{3\mu_s'}, \tag{8}$$

where the coefficient A, depending on the ratio of the refractive indices, is computed using Ref. [7]. The remaining term $\langle\Delta r^2(\tau)\rangle$ represents the mean squared displacement of the

moving scatterers. In the past, two main speed distributions, defining $\langle \Delta r^2(\tau)\rangle$, for the red blood cells moving in the microvascular network of a biological tissue, have been considered: 1) the Brownian movement ([3])

$$\langle \Delta r^2(\tau)\rangle = 6D_B\tau, \tag{9}$$

where D_B is the diffusion coefficient related to the scatterers' movement. In this case, the blood flow is proportional to $P_m D_B$; 2) the random movement ([3])

$$\langle \Delta r^2(\tau)\rangle = \langle V_R^2\rangle \tau^2, \tag{10}$$

where $\langle V_R^2\rangle$ is the second moment of the scatterers' speed. For the random model, the blood flow is proportional to $P_m\langle V_R^2\rangle$.

Equation (1) is utilized, in a normalized form ($G_{1\text{class}}(\rho,\tau)/G_{1\text{class}}(\rho,0)$), to fit the experimental data obtained from the hardware composing the optical flow meters and to extract tissue blood-flow values. If one carefully observes the quality of the fits on biological data, one rapidly realizes that the Brownian model is the better model. However, neither of the two models [Eqs. (9) and (10)] perfectly fits the data. This can be seen, e.g., in the figures appearing in Refs. [3,8–10] (note that in some figures the normalized intensity autocorrelation function $g_2(\rho,\tau) = 1 + |G_{1\text{class}}(\rho,\tau)/G_{1\text{class}}(\rho,0)|^2$, or the normalized field autocorrelation function $g_1(\rho,\tau) = G_{1\text{class}}(\rho,\tau)/G_{1\text{class}}(\rho,0)$, are represented in place of $G_{1\text{class}}(\rho,\tau)$). This is the reason why further speed models have been introduced with the aim to better fit the data [11], such as the mixed model [9,12] (linear combination of Brownian and random models) or the hydrodynamic diffusion (Langevin) model [8,13]. These models undoubtedly provide a better fit to the data. However, in some cases, no differences in the derived flow parameters have been observed if compared with the Brownian model [10]. It is important to note that these results might be simply due to the larger number of degrees of freedom owned by the mixed and the hydrodynamic diffusion model so that they "mathematically" fit more easily complex data shapes. This does not automatically mean that these more complex models do necessarily describe the actual underlying physics.

At this point, a basic question may be formulated: is Eq. (1) able to precisely describe the data when the investigated system, and in particular the speed distribution of the scatterers, are exactly known? In order to clarify this point, going back to the origin of Eq. (1), we can draw two important observations:

- Equation (1) has been derived from a correlation diffusion equation (CDE) where the parameter P_m has been introduced after its derivation "by hand" (see, e.g., [2]). In other words, the CDE was not directly derived from the more fundamental and general correlation transport equation (CTE), suitably taking into account the static background from the beginning. Therefore, the actual dependence on P_m might be more complex or different from the one appearing in Eq. (1).
- Equation (1) is used to describe a physical system represented by a semi-infinite medium, where the source/detector configuration is in reflectance mode. However, Eq. (1) has been derived by considering the detection of a *fluence rate* signal [14], while the actual measured signal is usually in *reflectance* configuration (fluence and reflectance solutions might not be exactly proportional in the present context).

The above two observations imply that Eq. (1) might not exactly fit *a fortiori* the amplitude and the shape of data obtained from a well-defined Brownian or random system. For these reasons, the aim of the present contribution was to clarify this problem. This has been done by deriving a new CDE from a CTE, taking simultaneously into account the moving scatterers and the static background. From the CDE, exact analytical solutions (ring and point-like detectors) for a semi-infinite medium in reflectance geometry have been obtained. The obtained solutions have been tested by comparisons with "gold standard" Monte Carlo (MC) simulations. Finally, the exact CDE solution for a point-like detector, $G_1(\rho,\tau)$, was compared to $G_{1\text{class}}(\rho,\tau)$. To simplify the reading, we will call from now on the solution for $G_1(\rho,\tau)$, the "reference CDE" solution, and $G_{1\text{class}}(\rho,\tau)$, the "classical CDE" solution.

2. METHODS

In Section 2.A, the CTE is presented. In Section 2.B, the main steps allowing one to derive the CDE from the CTE are explained. In Sections 2.C.1 and 2.C.2, the analytical solutions for a semi-infinite medium, with a point-like or a ring detector are derived. A comment on the MC code is presented in Section 2.D.

A. CTE

As previously demonstrated [15], the CTE for the directional electric field autocorrelation function, $G_1(\boldsymbol{r},\hat{\Omega},\tau)$ (W mm^{-2} sr^{-1}), can be expressed as

$$[\hat{\Omega}\cdot\nabla_{\boldsymbol{r}} + \mu_t]G_1(\boldsymbol{r},\hat{\Omega},\tau) = \mu_s\int F(\hat{\Omega}\cdot\hat{\Omega}',\tau)G_1(\boldsymbol{r},\hat{\Omega}',\tau)\mathrm{d}\Omega' + \frac{S_0\delta(\boldsymbol{r}-z_o\hat{z})}{4\pi}, \tag{11}$$

where

$$F(\hat{\Omega}\cdot\hat{\Omega}',\tau) = \{[g_{1,\text{single}}(\hat{\Omega}\cdot\hat{\Omega}',\tau) - 1]P_m + 1\}f(\hat{\Omega}\cdot\hat{\Omega}'). \tag{12}$$

Equation (11) holds for any speed distribution of the scatterers, and, through the term P_m, it also takes into account the presence of a static scattering background. The unit vector $\hat{\Omega}'$ describes the direction of a photon before the interaction with a moving scatterer and $\hat{\Omega}$ the direction after the interaction. The variable $\boldsymbol{r} = (x,y,z)$ (mm) is the spatial position. The notation $\hat{\Omega}\cdot\nabla_{\boldsymbol{r}}$ represents the scalar product between $\hat{\Omega}$ and the gradient operator. The total extinction or attenuation coefficient is expressed as $\mu_t = \mu_s + \mu_a$. The light source was set at a depth

$$z_0 = (\mu_a + (1-g)\mu_s)^{-1}, \tag{13}$$

where g is the mean cosine of the angle between $\hat{\Omega}$ and $\hat{\Omega}'$. Such a position of the source models an external pencil beam of unitary strength impinging normally onto the medium. The third term on the right hand side of Eq. (11) represents a unitary isotropic emitting point light source of 1 W mm^{-3} sr^{-1}, where $S_0 = 1$ W. The Dirac function $\delta(\cdot)$ has mm^{-3} units, and the factor 4π has steradian units. The function $f(\hat{\Omega}\cdot\hat{\Omega}')$ is the phase function. In the context of biomedical optics, $f(\hat{\Omega}\cdot\hat{\Omega}')$ is often the classical Henyey–Greenstein function, and this is also what we will adopt

here. The normalized field autocorrelation function for a single scattering event with a moving scatterer is [2]

$$g_{1,\text{single}}(\hat{\Omega}\cdot\hat{\Omega}',\tau)=e^{-a(1-\hat{\Omega}\cdot\hat{\Omega}')}. \tag{14}$$

The fundamental point to note is that Eq. (11) has exactly the same form as the classical radiative transport equation (RTE). Thus, all the procedures applied to derive the classical diffusion equation from the RTE can similarly be applied, step-by-step, to derive the CDE from the CTE. For this reason, and also due to the long procedure, in the following sections we will present only the main results in obtaining the CDE.

In this context, it is also worth noting that the CTE naturally derives from an approximation of a modified Bethe–Salpeter equation (BSE) [16]. The BSE equation directly follows from Maxwell theory and is more general than the CTE. In principle, it is possible to directly introduce P_m in the BSE, and then derive Eq. (11). In this sense, the results presented in the present contribution actually start from a more fundamental basis than Eq. (11).

B. Derivation of the CDE

The CDE can be derived from Eq. (11) by following step-by-step the analogous procedure found, for example, in Refs. [2,17]. Thus, the resulting CDE is

$$\mu_A G_1(\boldsymbol{r},\tau)-D_c\nabla^2 G_1(\boldsymbol{r},\tau)=\frac{S_0\delta(\boldsymbol{r}-z_o\hat{z})}{4\pi}, \tag{15}$$

where

$$G_1(\boldsymbol{r},\tau)=\int G_1(\boldsymbol{r},\hat{\Omega},\tau)\mathrm{d}\Omega, \tag{16}$$

$$\mu_A=\mu_s[1-F_0(\tau)]+\mu_a, \tag{17}$$

$$D_c=\frac{1}{3\{\mu_s[1-F_1(\tau)]+\mu_a\}}. \tag{18}$$

Equations (15–18) are formally the same as the classical diffusion equation, except for the terms $F_0(\tau)$ and $F_1(\tau)$, which, in the present case, are more complex and are expressed as

$$\begin{aligned}F_0(\tau)=&\frac{P_m}{2}\left\{\sqrt{\frac{a\pi}{2\,g^3}}(g^2-1)\right.\\&\times\left[\operatorname{erf}\left(\sqrt{\frac{a}{2g}}(g-1)\right)+\operatorname{erf}\left(\sqrt{\frac{a}{2g}}(g+1)\right)\right]e^{\frac{a(g-1)^2}{2g}}\\&\left.+\left(1-\frac{1}{g}\right)e^{-2a}+1+\frac{1}{g}\right\}+(1-P_m),\end{aligned} \tag{19}$$

$$\begin{aligned}F_1(\tau)=&\frac{P_m}{4}\left\{\sqrt{\frac{\pi}{2\,g^5 a}}(g^4a+g^3-a-g)\right.\\&\times\left[\operatorname{erf}\left(\sqrt{\frac{a}{2g}}(g-1)\right)+\operatorname{erf}\left(\sqrt{\frac{a}{2g}}(g+1)\right)\right]e^{\frac{a(g-1)^2}{2g}}\\&\left.-\left(1-g-\frac{1}{g}+\frac{1}{g^2}\right)e^{-2a}+1+g+\frac{1}{g}+\frac{1}{g^2}\right\}\\&+(1-P_m)g.\end{aligned} \tag{20}$$

Note that, by construction [15], when $\tau=0$, we must find the classical diffusion equation, and in fact $\lim_{\tau\to0^+}F_0(\tau)=1$ and $\lim_{\tau\to0^+}F_1(\tau)=g$ as it must be. The terms $F_0(\tau)$ and $F_1(\tau)$ were derived as

$$F_l(\tau)=2\pi\int_{-1}^{1}F(\zeta,\tau)P_l(\zeta)\mathrm{d}\zeta, \tag{21}$$

($l\in\{0,1\}$), where $P_l(\zeta)$ are the Legendre polynomials. Thus, other expressions for $F_0(\tau)$ and $F_1(\tau)$, corresponding to other types of phase function different from the Henyey–Greenstein, $f(\hat{\Omega}\cdot\hat{\Omega}')$, might be derived if necessary.

C. Solutions of the CDE for a Semi-Infinite Medium

Once the CDE [Eq. (15)] is known, we can in principle find $G_1(\boldsymbol{r},\tau)$ for any desired geometry of the medium and source/detector position. In the case of our semi-infinite medium, with the source and detector set at a distance ρ, the field autocorrelation function detected in reflectance mode, $G_1(\rho,\tau)$, can be obtained after solving Eq. (15) and then applying [18]

$$G_1(\rho,\tau)=D_c\frac{\partial}{\partial z}G_1(\boldsymbol{r},\tau)|_{z=0}. \tag{22}$$

The above formula represents Fick's law and is completely consistent with the diffusion equation. Equation (22) is strictly valid only in a diffusive regime.

1. CDE Solution for a Ring Detector Infinitely Thin

Thanks to the cylindrical symmetry of the problem (around the z axis; see Fig. 1), a point-like detector can be described as a ring detector infinitely thin. Thus, the solution for $G_1(\rho,\tau)$ in this case is [18]

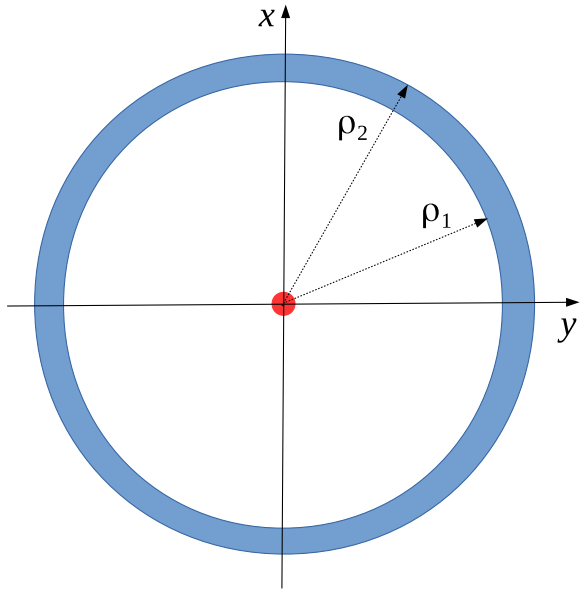

Fig. 1. Semi-infinite medium seen from the top. Right-handed coordinate system (z axis enters the plane). (**blue**), ring detector placed on the semi-infinite plane (at $z=0$); (**red**), isotropic emitting point light source at $z=(0,0,z_0)$ (under the plane).

$$G_1(\rho,\tau) = -\frac{1}{4\pi}\times\left(\frac{z_{3,0}}{(\rho^2+z_{3,0}^2)^{3/2}}\left\{1+\left[\frac{\mu_A(\rho^2+z_{3,0}^2)}{D_c}\right]^{1/2}\right\}\times\exp\left\{-\left[\frac{\mu_A(\rho^2+z_{3,0}^2)}{D_c}\right]^{1/2}\right\}-\frac{z_{4,0}}{(\rho^2+z_{4,0}^2)^{3/2}}\left\{1+\left[\frac{\mu_A(\rho^2+z_{4,0}^2)}{D_c}\right]^{1/2}\right\}\times\exp\left\{-\left[\frac{\mu_A(\rho^2+z_{4,0}^2)}{D_c}\right]^{1/2}\right\}\right), \tag{23}$$

where

$$z_{3,0} = -z_0, \tag{24}$$

$$z_{4,0} = 2z_e + z_0, \tag{25}$$

$$z_e = 2AD_c. \tag{26}$$

2. CDE Solution for a Ring Detector

If we want to test the present theory against reference MC simulations, we must take into account the fact that a MC detector can never be "infinitely thin" (actually also a real detector). For this reason, the solution $G_1(\rho_1,\rho_2,\tau)$ for a ring of finite thickness (see Fig. 1), delimited by ρ_1 and ρ_2, is also given [18]

$$G_1(\rho_1,\rho_2,\tau) = -\frac{1}{4\pi^{3/2}(\rho_2^2-\rho_1^2)D_c^{1/2}}\times\left\{z_{3,0}\sqrt{\frac{4\pi D_c}{\rho_1^2+z_{3,0}^2}}\exp\left[-2\sqrt{\frac{\mu_A(\rho_1^2+z_{3,0}^2)}{4D_c}}\right]-z_{4,0}\sqrt{\frac{4\pi D_c}{\rho_1^2+z_{4,0}^2}}\exp\left[-2\sqrt{\frac{\mu_A(\rho_1^2+z_{4,0}^2)}{4D_c}}\right]-z_{3,0}\sqrt{\frac{4\pi D_c}{\rho_2^2+z_{3,0}^2}}\exp\left[-2\sqrt{\frac{\mu_A(\rho_2^2+z_{3,0}^2)}{4D_c}}\right]+z_{4,0}\sqrt{\frac{4\pi D_c}{\rho_2^2+z_{4,0}^2}}\exp\left[-2\sqrt{\frac{\mu_A(\rho_2^2+z_{4,0}^2)}{4D_c}}\right]\right\}, \tag{27}$$

where ρ_1 (mm) and ρ_2 (mm) are the minimum and maximum radius of the ring. This detector geometry is largely utilized in classical MC simulations such as the well-known Monte Carlo multi-layered (MCML) [19]. Note that $\lim_{\rho_1\to\rho_2=\rho} G_1(\rho_1,\rho_2,\tau) = G_1(\rho,\tau)$. Thus, in the present context, if the tests for $G_1(\rho_1,\rho_2,\tau)$ are valid, then they are also valid for $G_1(\rho,\tau)$.

D. MC Code

The "gold standard" MC data have been generated with the code previously used in Ref. [15] to test the CTE. To be compatible with Eq. (27), the position of the isotropic light source was set to $(0, 0, z_0)$ [Eq. (13)]. However, it is important to note that, in the diffusive regime and for large ρ, MC simulations made with a light pencil beam reproducing a situation more similar to real experimental conditions, give almost the same results [20]. Simulations have been performed on a computer cluster with 12 nodes. For each MC simulation (i.e., one $G_1(\rho_1,\rho_2,\tau)$ curve) 10^7 photon packets have been generated. To obtain an estimation of the standard deviation, the same MC simulation has been repeated five times. MC simulations have been performed for a wide range of parameters, but only some representative results have been reported in the Results section.

3. RESULTS

In Fig. 2, MC simulations, together with the corresponding analytical solutions computed with Eq. (27), are shown. As expected from the CTE theory that is behind the CDE equation, the analytical curves agree with the MC data. The CDE analytical model is also able to reproduce situations where the number of moving scatterers is low ($P_m \ll 1$) and where for large τ, $G_1(\rho_1,\rho_2,\tau)$ never goes to zero (see, e.g., the magenta line). This is the case because, intuitively, the contribution on $G_1(\rho_1,\rho_2,\tau)$ from the photons that did not interact with a moving scatterer does not "decorrelate". The CDE [Eq. (27)] works for both the Brownian [Eq. (9), red and blue lines] or the random flow [Eq. (10), green and yellow lines]. Thus, in principle, it is not necessary to search for new equations for these two conditions. From these results also ensues the validity of $G_1(\rho,\tau)$ [Eq. (23)]. In fact, as has already been mentioned in Section 2.C.2, $G_1(\rho,\tau)$ is the limit of $G_1(\rho_1,\rho_2,\tau)$, in the case $\rho_1\to\rho^-$ and $\rho_2\to\rho^+$. This is an important observation, because it is assumed that $G_1(\rho,\tau)$ describes the same physical model as the classical $G_{1\text{class}}(\rho,\tau)$ [Eq. (1)]. Thus, the function $G_1(\rho,\tau)$ can be used as a reference (equivalent to a MC simulation, but a lot faster) to verify the validity of $G_{1\text{class}}(\rho,\tau)$.

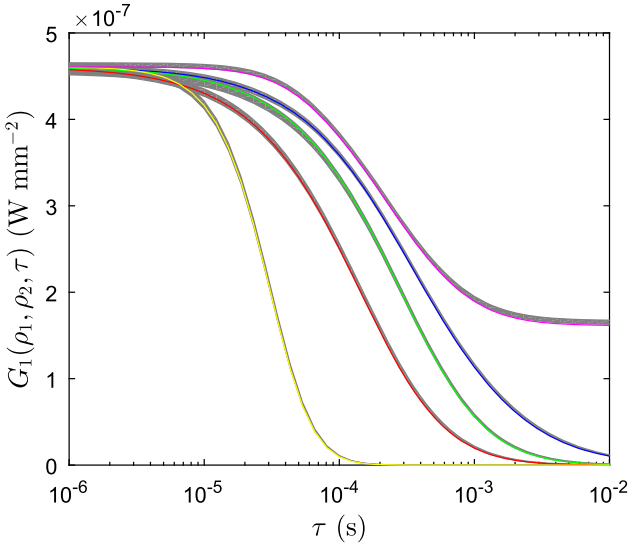

Fig. 2. Analytical solutions [**colored**; Eq. (27)] compared to the MC solutions (**gray**; covered by the colored lines). The variable thickness of the gray lines corresponds to two standard deviations. Common parameters are $\mu_a = 0.025$ mm^{-1}, $\mu_s' = 1$ mm^{-1}, $n = 1.4$, $g = 0.9$, $\lambda = 785$ nm, $\rho_1 = 21.22$ mm, and $\rho_2 = 24.33$ mm. (**red**), Brownian model, $P_m = 0.025$, $D_B = 1\times10^{-5}$ mm^2 s^{-1}; (**blue**), Brownian model, $P_m = 0.01$, $D_B = 1\times10^{-5}$ mm^2 s^{-1}; (**green**), Brownian model, $P_m = 0.025$, $D_B = 0.5\times10^{-5}$ mm^2 s^{-1}; (**yellow**), random model, $P_m = 0.025$, $\langle V_R^2\rangle = 3$ mms^{-1}; (**magenta**), random model, $P_m = 0.001$, $\langle V_R^2\rangle = 3$ mms^{-1}.

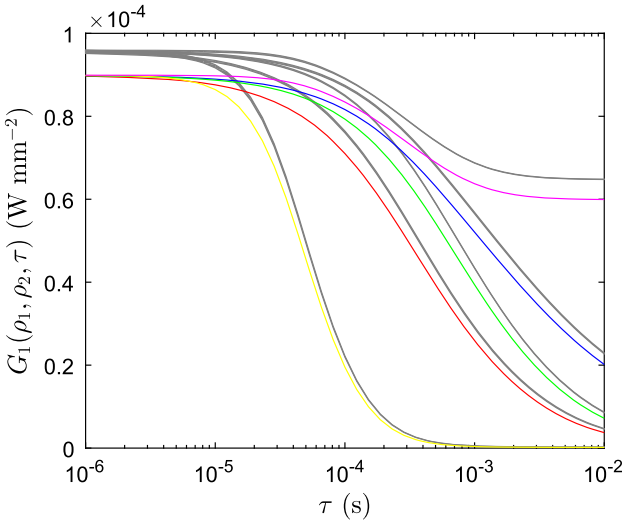

Fig. 3. Same optical parameters and symbols as in Fig. 2, with the only difference being that $\rho_1 = 8.86$ mm and $\rho_2 = 10.10$ mm.

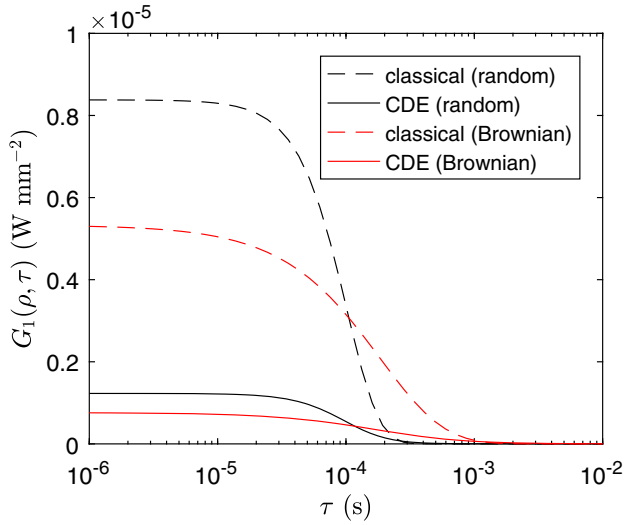

Fig. 4. Reference CDE solution Eq. (23) (continuous lines) compared to the classical CDE solution Eq. (1) (dashed lines). Common parameters are: $\mu_s' = 1$ mm^{-1}, $n = 1.4$, $g = 0.8$, $\lambda = 785$ nm, and $\rho = 20$ mm. (**black**), $\mu_a = 0.025$ mm^{-1}, $P_m = 0.025$, $\langle V_R^2 \rangle = 1$ mms^{-1}; (**red**), $\mu_a = 0.03$ mm^{-1}, $P_m = 0.025$, $D_B = 1 \times 10^{-5}$ mm^2 s^{-1}.

Figure 3 shows some examples where the condition of diffusion regime is broken. This was obtained by using the same parameter values as in Fig. 2, but with a source/detector separation of ≈9 mm. From the MC simulations, it clearly appears that the $G_1(\rho_1, \rho_2, \tau = 0)$ reflectance values are larger than in Fig. 2, obviously because more photons reach the detector. Moreover, the fraction of nonscattered photons on a moving scatterer, represented by $G_1(\rho_1, \rho_2, \tau = +\infty)/G_1(\rho_1, \rho_2, \tau = 0)$, is also higher than in Fig. 2. In fact, the photons that travel on a shorter path interact with fewer moving scatterers. As expected, it clearly appears that when the diffuse regime condition is broken, the CDE model does not hold anymore (colored curves do not reproduce the absolute MC data). It is important to note that, in order to account for situations at the limit of the diffusive regime, the present approach might be implemented by exploiting other "improved" diffusion models such as, e.g., the one proposed in Ref. [21]. Of course, at extremely short source/detector separation, the exact CTE theory must be used [15]. However, the CTE approach is less easy to be implemented in an instrument with real-time data analysis for blood-flow measurements. The latter two approaches are obviously thought to be used beyond the diffusive regime, and thus they are out of the frame of the present contribution.

In Fig. 4, $G_1(\rho, \tau)$ and $G_{1\text{class}}(\rho, \tau)$ are compared for two different sets of optical parameters values. It is clear that, compared to the reference $G_1(\rho, \tau)$, the amplitude of $G_{1\text{class}}(\rho, \tau)$ is too large. As already explained in Section 1, this is due to the fact that in deriving $G_{1\text{class}}(\rho, \tau)$, the reflectance mode was not considered. In practice, Eq. (22) has not been applied to $G_{1\text{class}}(\rho, \tau)$, and this may explain the different scaling factor. However, this might not be a problem from an experimental point of view. In fact, in practice $G_{1\text{class}}(\rho, \tau)$ is never directly used as it is, and only its normalized version (normalized electric field autocorrelation function)

$$g_1(\rho, \tau) = \frac{G_{1\text{class}}(\rho, \tau)}{G_{1\text{class}}(\rho, 0)}, \tag{28}$$

appears in the literature. The same expression obviously holds for $G_1(\rho, \tau)$,

$$g_1(\rho, \tau) = \frac{G_1(\rho, \tau)}{G_1(\rho, 0)}, \tag{29}$$

[in Eqs. (28) and (29) we use the same notation, $g_1(\rho, \tau)$, for simplicity; let the context clarify the meaning]. Thus, if it were only a problem of scaling factor, the simpler expression for $G_{1\text{class}}(\rho, \tau)$ could be suitably used to treat the experimental data as it is usually done. Let us see if this is the case.

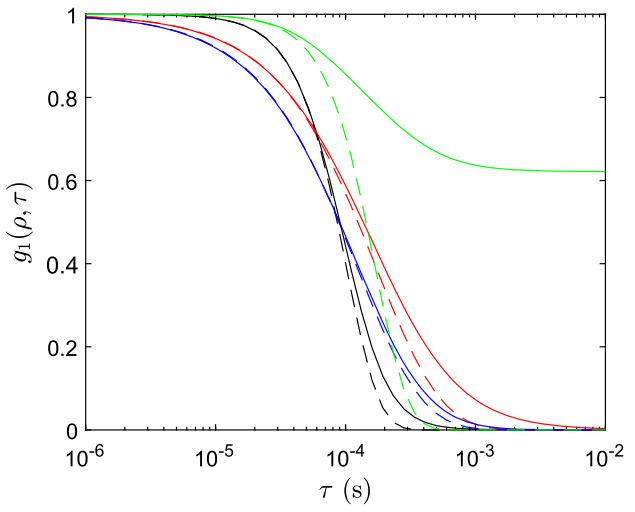

Fig. 5. Normalized electric field autocorrelation function, $g_1(\rho, \tau)$, obtained with the reference CDE [Eq. (23), continuous lines] and the classical CDE [Eq. (1), dashed lines]. Common parameters are: $\mu_a = 0.025$ mm^{-1}, $\mu_s' = 1$ mm^{-1}, $n = 1.4$, $g = 0.8$, $\lambda = 785$ nm, and $\rho = 20$ mm. (**black**), random model, $P_m = 0.025$, $\langle V_R^2 \rangle = 1$ mms^{-1}; (**red**), Brownian model, $P_m = 0.025$, $D_B = 1 \times 10^{-5}$ mm^2 s^{-1}; (**blue**), Brownian model, $P_m = 0.07$, $D_B = 0.5 \times 10^{-5}$ mm^2 s^{-1}; (**green**), random model, $P_m = 0.001$, $\langle V_R^2 \rangle = 3$ mms^{-1}.

In Fig. 5, $g_1(\rho,\tau)$ computed with the classical [Eq. (1)] and the reference [Eq. (23)] CDE models are compared for different sets of optical parameters values. From the figure, it can be concluded that the difference between the two models is not only due to a simple scaling factor. In fact, the classical (normalized) model is not able to take into account the case of small P_m (green lines), because it always goes to the zero baseline even when $g_1(\rho,\tau=+\infty)$ actually does not go to zero. In general, the classical model underestimates the reference curves. These findings are also compatible with the observations reported in the literature [3,8–10] and can be one of the reasons for the differences between experimental data and the classical mathematical model. It is possible to conclude that, in the present context, the dependence on P_m is actually more complex than the one classically described by $G_{1\text{class}}(\rho,\tau)$. For the sake of completeness, we note that by using a reflectance model obtained with the classical approach and "improved" boundary conditions, the obtained solutions, for large P_m values, are compatible with the MC data [22]. In fact, when P_m becomes large, $G_1(\rho,\tau=+\infty)$ always goes to zero, and the error on the shape of the curve tends to decrease (see, e.g., blue curve in Fig. 5), and the models become equal.

4. DISCUSSION AND CONCLUSIONS

In the present contribution, a CDE has been directly derived from a CTE capable of describing the propagation of light in a medium containing both moving scatterers and static background. Explicit analytical solutions, for a semi-infinite medium with a point light source and a point-like or ring detector, positioned in reflectance geometry, have been obtained. It has been shown that the reference model reproduces the "gold standard" MC data. It has also been demonstrated that the dependence on P_m is more complex than the one described by the classical CDE model, historically derived from a CDE where the P_m parameter was introduced by following a more phenomenological approach [6]. This observation might be of interest for tissues such as human bone, where the P_m values are probably very low [23], and thus more precise models, such as the proposed reference CDE, are necessary. In fact, bone tissue is composed in part of inert/mineral components that behave as a static background. The proposed model might allow us to better investigate this important topic in the future. The proposed approach can also be implemented for other geometries such as multilayered media ([24]), or for other types of light sources such as, e.g., the pencil beam. Equations (23) or (27) may also be used to fit the experimental data, where P_m and D_B (or $\langle V_R^2\rangle$) appear as fitting parameters (it is in principle impossible to separate them in the "classical" model). To improve the fitting procedure, some constraints may be included in the algorithm such as, e.g.,: $0 \le P_m \le 1$, $D_B > 0$ or $\langle V_R^2\rangle > 0$. It is clear that investigations on the stability of the fitting procedure must be matter for future studies. In conclusion, we hope that the present analytical models will be a useful and easy-to-use reference, allowing researchers to test/develop new blood flow-related algorithms in the diffusion regime.

REFERENCES

1. D. A. Boas, L. E. Campbell, and A. G. Yodh, "Scattering and imaging with diffusing temporal field correlations," Phys. Rev. Lett. **75**, 1855–1858 (1995).
2. D. A. Boas, "Diffuse photon probes of structural and dynamical properties of turbid media: theory and biomedical applications," Ph.D. dissertation (University of Pennsylvania, 1996).
3. T. Durduran, R. Choe, W. B. Baker, and A. G. Yodh, "Diffuse optics for tissue monitoring and tomography," Rep. Prog. Phys. **73**, 076701 (2010).
4. M. Ninck, M. Untenberger, and T. Gisler, "Diffusing-wave spectroscopy with dynamic contrast variation: disentangling the effects of blood flow and extravascular tissue shearing on signals from deep tissue," Biomed. Opt. Express **1**, 1502–1513 (2010).
5. M. Diop, K. Verdecchia, T.-Y. Lee, and K. S. Lawrence, "Calibration of diffuse correlation spectroscopy with a time-resolved near-infrared technique to yield absolute cerebral blood flow measurements," Biomed. Opt. Express **2**, 2068–2081 (2011).
6. D. Boas and A. Yodh, "Spatially varying dynamical properties of turbid media probed with diffusing temporal light correlation," J. Opt. Soc. Am. A **14**, 192–215 (1997).
7. D. Contini, F. Martelli, and G. Zaccanti, "Photon migration through a turbid slab described by a model based on diffusion approximation, I: theory," Appl. Opt. **36**, 4587–4599 (1997).
8. S. A. Carp, N. Roche-Labarbe, M. A. Franceschini, V. J. Srinivasan, S. Sakadžić, and D. A. Boas, "Due to intravascular multiple sequential scattering, diffuse correlation spectroscopy of tissue primarily measures relative red blood cell motion within vessels," Biomed. Opt. Express **2**, 2047–2054 (2011).
9. H. M. Varma, C. P. Valdes, A. K. Kristoffersen, J. P. Culver, and T. Durduran, "Speckle contrast optical tomography: a new method for deep tissue three-dimensional tomography of blood flow," Biomed. Opt. Express **5**, 1275–1289 (2014).
10. K. Verdecchia, M. Diop, L. B. Morrison, T. Y. Lee, and K. St. Lawrence, "Assessment of the best flow model to characterize diffuse correlation spectroscopy data acquired directly on the brain," Biomed. Opt. Express **6**, 4288–4301 (2015).
11. T. Binzoni and F. Martelli, "Assessing the reliability of diffuse correlation spectroscopy models on noise-free analytical Monte Carlo data," Appl. Opt. **54**, 5320–5326 (2015).
12. D. A. Boas, S. Sakadžić, J. Selb, P. Farzam, M. A. Franceschini, and S. A. Carp, "Establishing the diffuse correlation spectroscopy signal relationship with blood flow," Neurophotonics **3**, 031412 (2016).
13. B. J. Berne and R. Pecora, *Dynamic Light Scattering: With Applications to Chemistry, Biology, and Physics* (Dover, 2000).
14. T. Durduran, "Non-invasive measurements of tissue hemodynamics with hybrid diffuse optical methods," Ph.D. dissertation (University of Pennsylvania, 2004).
15. T. Binzoni, A. Liemert, A. Kienle, and F. Martelli, "Analytical solution of the correlation transport equation with static background: beyond diffuse correlation spectroscopy," Appl. Opt. **55**, 8500–8505 (2016).
16. R. Pierrat, "Transport equation for the time correlation function of scattered field in dynamic turbid media," J. Opt. Soc. Am. A **25**, 2840–2845 (2008).
17. I. Bigio and S. Fantini, *Quantitative Biomedical Optics: Theory, Methods, and Applications*, Cambridge Texts in Biomedical Engineering (Cambridge University, 2016).
18. F. Martelli, S. del Bianco, A. Ismalelli, and G. Zaccanti, *Light Propagation through Biological Tissue and Other Diffusive Media: Theory, Solutions, and Software* (SPIE, 2010).
19. L. H. Wang, S. Jacques, and L. Q. Zheng, "MCML-Monte–Carlo modeling of light transport in multilayered tissues," Comput. Methods Programs Biomed. **47**, 131–146 (1995).
20. T. J. Farrell, M. S. Patterson, and B. Wilson, "A diffusion theory model of spatially resolved, steady-state diffuse reflectance for the noninvasive determination of tissue optical properties *in vivo*," Med. Phys. **19**, 879–888 (1992).

21. A. Kienle and M. S. Patterson, "Improved solutions of the steady-state and the time-resolved diffusion equations for reflectance from a semi-infinite turbid medium," J. Opt. Soc. Am. A **14**, 246–254 (1997).
22. A. Kienle, "Non-invasive determination of muscle blood flow in the extremities from laser Doppler spectra," Phys. Med. Biol. **46**, 1231–1244 (2001).
23. T. Binzoni, B. Sanguinetti, D. Van de Ville, H. Zbinden, and F. Martelli, "Probability density function of the electric field in diffuse correlation spectroscopy of human bone *in vivo*," Appl. Opt. **55**, 757–762 (2016).
24. A. Liemert and A. Kienle, "Light diffusion in N-layered turbid media: steady-state domain," J. Biomed. Opt. **15**, 025003 (2010).